metals

MDPI

Article

Graphite/Epoxy-Coated Flaky FeSiCr Powders with Enhanced Microwave Absorption

Haonan Zhang [1], Xichun Zhong [1,*], Jinwen Hu [1], Na He [1], Hanxing Xu [1], Xuefeng Liao [2], Qing Zhou [2], Zhongwu Liu [1] and Raju V. Ramanujan [3]

[1] School of Materials Science and Engineering, South China University of Technology, Guangzhou 510641, China; 202120121423@mail.scut.edu.cn (H.Z.); 202110184223@mail.scut.edu.cn (J.H.); 202010103946@mail.scut.edu.cn (N.H.); 202121023124@mail.scut.edu.cn (H.X.); zwliu@scut.edu.cn (Z.L.)
[2] Guangdong Provincial Key Laboratory of Rare Earth Development and Application, Institute of Resources Utilization and Rare Earth Development, Guangdong Academy of Sciences, Guangzhou 510650, China; liaoxuefeng@grre.gd.cn (X.L.); zqwork@grre.gd.cn (Q.Z.)
[3] School of Materials Science and Engineering, Nanyang Technological University, Singapore 639798, Singapore; ramanujan@ntu.edu.sg
* Correspondence: xczhong@scut.edu.cn

Abstract: Flake-shaped FeSiCr (FFSC) material is expected to be a promising microwave absorbent due to its excellent magnetic properties and environmental resistance. By introducing carbon-based materials through suitable coatings, the electromagnetic parameters and energy loss can be tuned to improve the performance of FFSC. A facile solution-blending method was deployed to prepare graphite- and epoxy resin-encapsulated FFSC (FFSC@G/E) powders with a core–shell structure. FFSC@G_{2000}/E showed excellent performance in the X band (8–12 GHz), a minimum reflection loss (RL_{min}) of −42.77 dB at a thickness of 3 mm and a maximum effective absorption bandwidth (EAB_{max}, RL < −10 dB) that reached 4.55 GHz at a thickness of 2.7 mm. This work provides a route for the production of novel high-performance microwave absorbers.

Keywords: fake-shaped FeSiCr material; carbon materials; coating; microwave absorption

Citation: Zhang, H.; Zhong, X.; Hu, J.; He, N.; Xu, H.; Liao, X.; Zhou, Q.; Liu, Z.; Ramanujan, R.V. Graphite/Epoxy-Coated Flaky FeSiCr Powders with Enhanced Microwave Absorption. *Metals* **2023**, *13*, 1611. https://doi.org/10.3390/met13091611

Academic Editor: Cristiano Fragassa

Received: 15 August 2023
Revised: 15 September 2023
Accepted: 16 September 2023
Published: 18 September 2023

1. Introduction

The high importance of stealth technology in the military field and of electromagnetic (EM) interference in the civilian field has resulted in extensive research on microwave-absorbing materials (MAMs). Thinner, lighter, wider, stronger MAMs with good service performance are urgently required [1–3].

Among the various MAMs developed, ferromagnetic metals (Fe, Co, Ni) and their alloys are most widely used in the microwave absorption field. Compared with dielectric and ferrite absorbers, ferromagnetic alloys possess better magnetic properties and more appropriate EM parameters, which are beneficial for their microwave absorption properties (MAP) [4,5]. The FeSiCr alloy powder is one such ferromagnetic MAM alloy with high permeability, high saturation magnification and high Curie temperature; in addition, the presence of Si and Cr improves its corrosion resistance and oxidation resistance [6,7]. Furthermore, through flake-shaped deformation induced by the ball milling process, the Snoek's limit of FeSiCr can be overcome to obtain higher permeability in the GHz band by improving planar anisotropy, inhibit the eddy current and skin effect of magnetic alloys and achieve a larger specific surface area that enhances dielectric loss (including conduction loss and polarization loss) in the absorbent [8–12]. Moreover, the parallel alignment of the flaky particles under an applied magnetic field can enhance the advantages of ultrahigh permeability and strong dielectric losses, providing the flaky FeSiCr (FFSC) material with excellent MAP [13,14].

The introduction of a carbon coating is another effective strategy to improve the MAP of magnetic alloys [15–22] due to the following effects. Firstly, carbon materials can provide

high dielectric loss owing to their special electronic structure, low dimensional structure and high density of defects, which increase the microwave loss pathways for the alloys [23,24]. Secondly, magnetic–dielectric composites possess tunable EM parameters, which is helpful for the optimization of impedance matching [3,25,26]. Thirdly, the heterostructures provide multiple polarization and scattering processes at core–shell interfaces [27,28]. For instance, Zhou et al. synthesized Ni/NiO@C by hydrothermal reduction and heat treatment methods, and the resulting sample showed a low minimum reflection loss (RL_{min}) of −51.1 dB at a thickness of 2.4 mm and a high maximum effective absorption bandwidth (EAB_{max}, RL < −10 dB) of 5.12 GHz at 2.7 mm of thickness [15]. Tian et al. prepared FeSiAl@SiO_2@C by the Stöber method and by catalytic chemical vapor deposition technology, and the resulting RL_{min} was as low as −46.29 dB at 16.93 GHz and 2.0 mm of thickness, while the EAB_{max} reached 7.33 GHz at 2.5 mm of thickness [16]. Other works on carbon-coated magnetic MAMs, such as Fe@C [17], $NiFe_2O_4$@Ni@C [19], CoNi@NC [20], $CoFe_2O_4$/CoFe@C [21] and Co/CoO/rGO, also reported excellent MAP [22].

Although great progress has been made in carbon-coated magnetic MAMs, issues including disordered microstructures, random dispersion and oxidation of alloys are inevitable for carbon-coated magnetic materials obtained by the pyrolysis of polymer-coated metallic oxides or hydroxide precursors [3,28]. Meanwhile, the strict process conditions such as high temperatures, inert atmosphere as well as a long synthesis time are not suitable for the manufacture of core–shell MAMs. Therefore, it is necessary to develop a physical coating method for magnetic powders. For example, Weng et al. prepared carbonyl iron/rGO/PVP by mechanical stirring in an aqueous solution, and the resulting sample displayed an excellent EAB_{max} of 13.8 GHz [4].

Here, to obtain a reliable carbon coating for FFSC at room temperature, epoxy resin was introduced as a "glue" between graphite and the alloy particles, and a simple solution-blending method was deployed to prepare FFSC@graphite/epoxy (FFSC@G/E) core–shell MAMs at room temperature. The effects of the presence of graphite and epoxy resin, as well as the effect of the particle size of graphite in FFSC@G/E were studied. The results showed that the sample of FFSC coated with graphite of 2000 mesh and epoxy (FFSC@G_{2000}/E) exhibited the best MAP, with an RL_{min} of −42.77 dB at 8.46 GHz at the thickness of 3 mm and an EAB_{max} of 4.55 GHz at the thickness of 2.7 mm.

2. Materials and Methods

The raw flaky $Fe_{87}Si_{11}Cr_2$ powders were purchased from Ganzhou Lanhai New materials Co., Ltd. (Ganzhou, China). The silane coupling agent (KH550) was purchased from Jiangxi Chenguang New materials Co., Ltd. (Jiujiang, China). The flake-shaped graphite powders (99.95%) with various particle sizes (1200 mesh, 2000 mesh and 5000 mesh) were purchased from Shanghai Macklin Biochemical Co. Ltd. (Shanghai, China). Epoxy resin (E-44) was purchased from Nantong Xingchen Synthetic Material Co., Ltd. (Nantong, China).

As illustrated in Figure 1, the preparation process of FFSC@G/E included coupling treatment and solution blending; the process was conducted at room temperature. Firstly, 50 g of solution composed of ethanol, deionized water and KH550 at the mass ratio of 18:5:2 was placed into a beaker containing 5 g of FFSC powders, and the mixture was stirred for 0.5 h. The function of the coupling treatment is to disperse the FFSC particles and improve the compatibility between the surface of FFSC and organic compounds [29]. After removing the coupling solution by magnetic separation, 0.25 g of graphite powders and 20 g of an acetone solution with 0.50 g of epoxy resin dissolved in it was added into the beaker. By rapid mechanical stirring, the components of FFSC, graphite and epoxy were sufficiently blended, while the acetone solvent fully vaporized in around 1.5 h. The coating-modified FFSC was then dried at 40 °C for 1 h and sieved by a 50-mesh screen sieve. The graphite samples with various particle sizes were denoted as G_{1200}, G_{2000} and G_{5000}. The samples of FFSC coated with epoxy (without the addition of graphite in the solution

blending process) and of FFSC coated with epoxy and graphite with different particle sizes were denoted as FFSC@E, FFSC@G_{1200}/E, FFSC@G_{2000}/E and FFSC@G_{5000}/E, respectively.

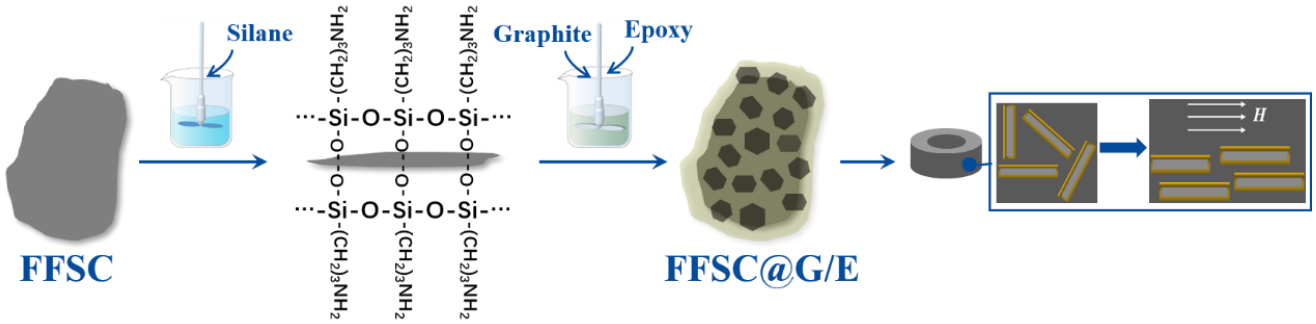

Figure 1. Schematic illustration of the preparation of the FFSC@G/E samples and the coaxial rings.

The phase composition of the magnetic powder and graphite powder samples was measured by X-ray diffraction (XRD, X'Pert Pro M, PANalytical, Eindhoven, The Netherlands) using Cu Kα radiation (λ = 1.54059 Å). The Raman spectra of the graphite samples were recorded by a laser Raman spectrometer (LabRAM Aramis, Horiba Jobin Yvon, Longjumeau, France) at a laser wavelength of 532 cm^{-1}. The particle size distribution of the samples was analyzed by a laser particle size analyzer (BT-9300ST, Bettersize, Dandong, China). The morphology of the samples and the elemental distribution were observed by scanning electron microscopy (SEM, Hitachi SU8220, Tokyo, Japan). The magnetic properties of the samples were determined by a vibrating sample magnetometer (VSM, MPMS-XL-7, Quantum Design, San Diego, CA, USA) at room temperature. The electromagnetic parameters of the samples were measured by a vector network analyzer (VNA, N5224B, Agilent, Santa Clara, CA, USA) using the coaxial line method over a frequency range of 0.5–18 GHz. A homogeneous mixture of the as-prepared powders and paraffin wax with a filler loading of 30 wt.% was pressed in a mold and formed coaxial rings with an external diameter of 7.00 mm, an internal diameter of 3.04 mm and a thickness of 2–3 mm under an applied magnetic field (Figure 1). The MAP of the samples was calculated based on the results of the VNA test. The conductivity of the coaxial ring samples was measured by a high-resistance weak current tester (ST2643, Suzhou Jingge Electronic Co., Ltd., Suzhou, China).

3. Results and Discussion

The XRD patterns of the graphite samples and the magnetic powder samples are shown in Figure 2a. Three graphite samples exhibited a sharp diffraction peak at 26.5° corresponding to the (002) crystal plane of the hexagonal graphite phase (PDF No. 03-065-6212), indicating their high degree of crystallization. For the three FFSC@G/E samples, the diffraction peak at 26.5° showed the presence of graphite, which did not appear in the patterns of FFSC and FFSC@E. For all magnetic powder samples, the diffraction peaks at 45.1°, 65.8°, 83.3° corresponded to the (110), (200), (211) crystal planes of the body-centered cubic α-Fe (Si,Cr) phase (PDF No. 00-001-1267). The degree of crystallization of graphite was quantitively characterized by the intensity ratio of the D peak and the G peak (I_D/I_G) in the Raman spectra (Figure 2b); the D peak appearing at 1346 cm^{-1} was due to amorphous carbon with sp^3 hybridization, while the G peak appearing at 1574 cm^{-1} represented graphitized carbon with sp^2 hybridization. Three graphite samples presented low values of the I_D/I_G ratio (0.141, 0.205 and 0.156) due to their high degree of crystallization. Amorphous carbon can reduce electrical conductivity and introduce point defects, thus enhancing impedance matching and dipole relaxation [30,31].

Figure 2c,d reveal the particle size distribution of the graphite and magnetic powder samples, respectively. The median particle sizes (D_{50}) of G_{1200}, G_{2000} and G_{5000} were 12.62 μm, 8.55 μm and 6.36 μm, respectively (Figure 2c), in agreement with the labeled particle sizes of the graphite samples. The D_{50} of FFSC, FFSC@E, FFSC@G_{1200}/E, FFSC@G_{2000}/E

and FFSC@G_{5000}/E were 70.62 μm, 120.3 μm, 119.4 μm, 114.4 μm and 116.5 μm, respectively (Figure 2d), and the particle size of FFSC exhibited a distinct increase after being coated with graphite and epoxy.

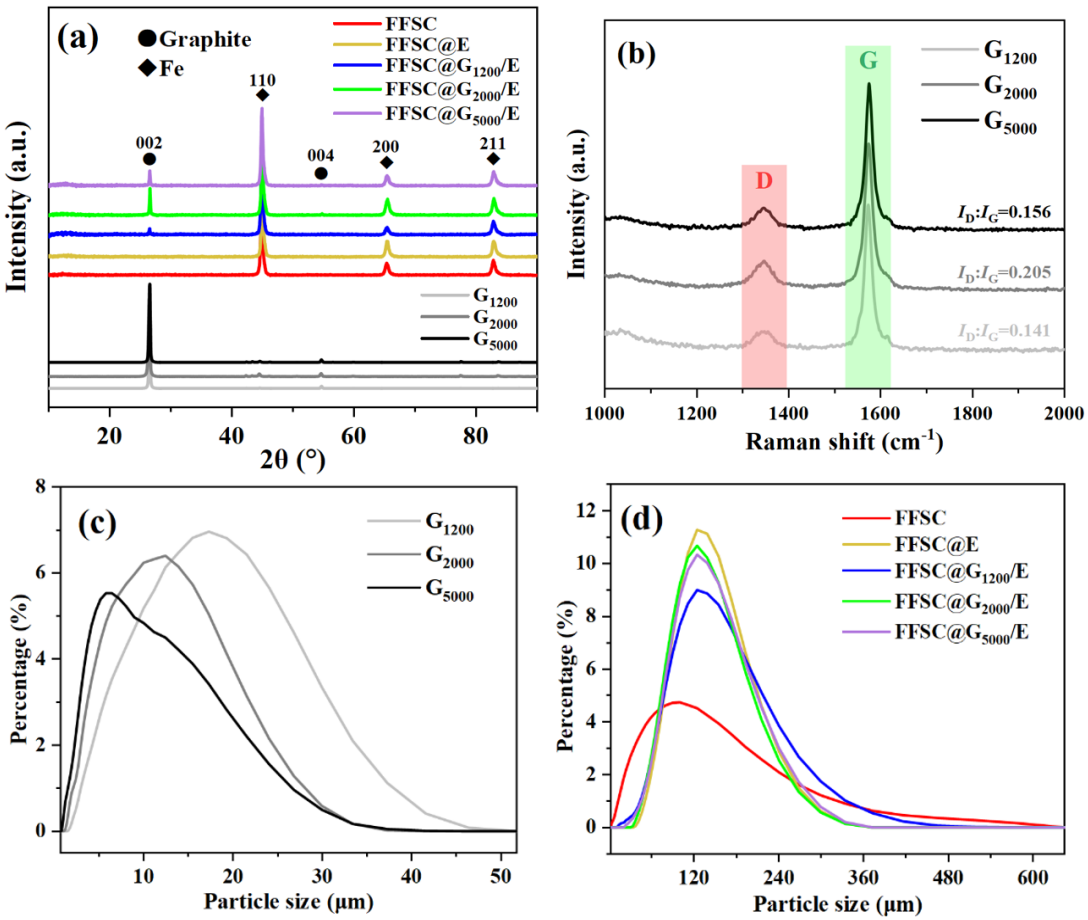

Figure 2. (**a**) XRD patterns of the graphite and magnetic powder samples; (**b**) Raman spectra of the graphite samples; (**c**) particle size distribution of the graphite samples; (**d**) particle size distribution of the magnetic powder samples.

SEM was deployed to observe the morphology of the magnetic powder samples. The well-dispersed original FFSC particles exhibited flaky outlines and smooth surfaces (Figure 3a,d), while agglomeration took place in the samples of FFSC@E and FFSC@G/E with rough surfaces and larger particle sizes, due to the coating and adhesion of epoxy on FFSC (Figure 3b,c), which was consistent with the results of the particle size distribution studies (Figure 2d).

The high-magnification image of the FFSC@E sample in Figure 3e shows that the folds of the epoxy layer were wrapped around the surfaces of FFSC (Figure 3e). For three FFSC@G/E samples (Figure 3g–i), small and dark particles corresponding to graphite (Figure 3f) can be seen deposited on the surfaces of the FFSC flakes, indicating that the graphite particles were attached to the surface of the magnetic particles through adhesive bonding with the epoxy coating. In addition, the density of distribution of graphite increased for lower particle sizes (Figure 3g–i). The EDS elemental mapping results of FFSC@G/E showed that the C signal was concentrated at the location of the dark particles (Figure 3j–l), confirming the successful coating by epoxy and graphite.

Figure 4a presents the magnetostatic properties of the magnetic powder samples. The FFSC sample had S-shape hysteresis loops and low coercivity, exhibiting typical soft magnetic characteristics. The saturation magnetization (M_S) of FFSC reached 175.8 emu/g, while the M_S values of FFSC@E, FFSC@G_{1200}/E, FFSC@G_{2000}/E and FFSC@G_{5000}/E

dropped to 141.4, 145.9, 154.1 and 152.8 emu/g, respectively, after the introduction of the graphite/epoxy coating, but still remained at relatively high values. For the hysteresis loops near 0 Oe, the slope of FFSC@G/E decreased compared with those of FFSC and FFSC@E due to the introduction of the diamagnetic graphite powders. The conductivity (σ) of the coaxial ring samples (Figure 4b) showed a good insulation of the absorbers due to the low filler loading of the magnetic powders, which is helpful for the inhibition of the skin effect [32]. Similar to the variation of M_S, the σ value of the magnetic powder/paraffin composites decreased from 8.13 pS/m to 2.84, 6.63, 7.11 and 4.67 pS/m for FFSC@E, FFSC@G_{1200}/E, FFSC@G_{2000}/E and FFSC@G_{5000}/E, respectively, after the coating of FFSC.

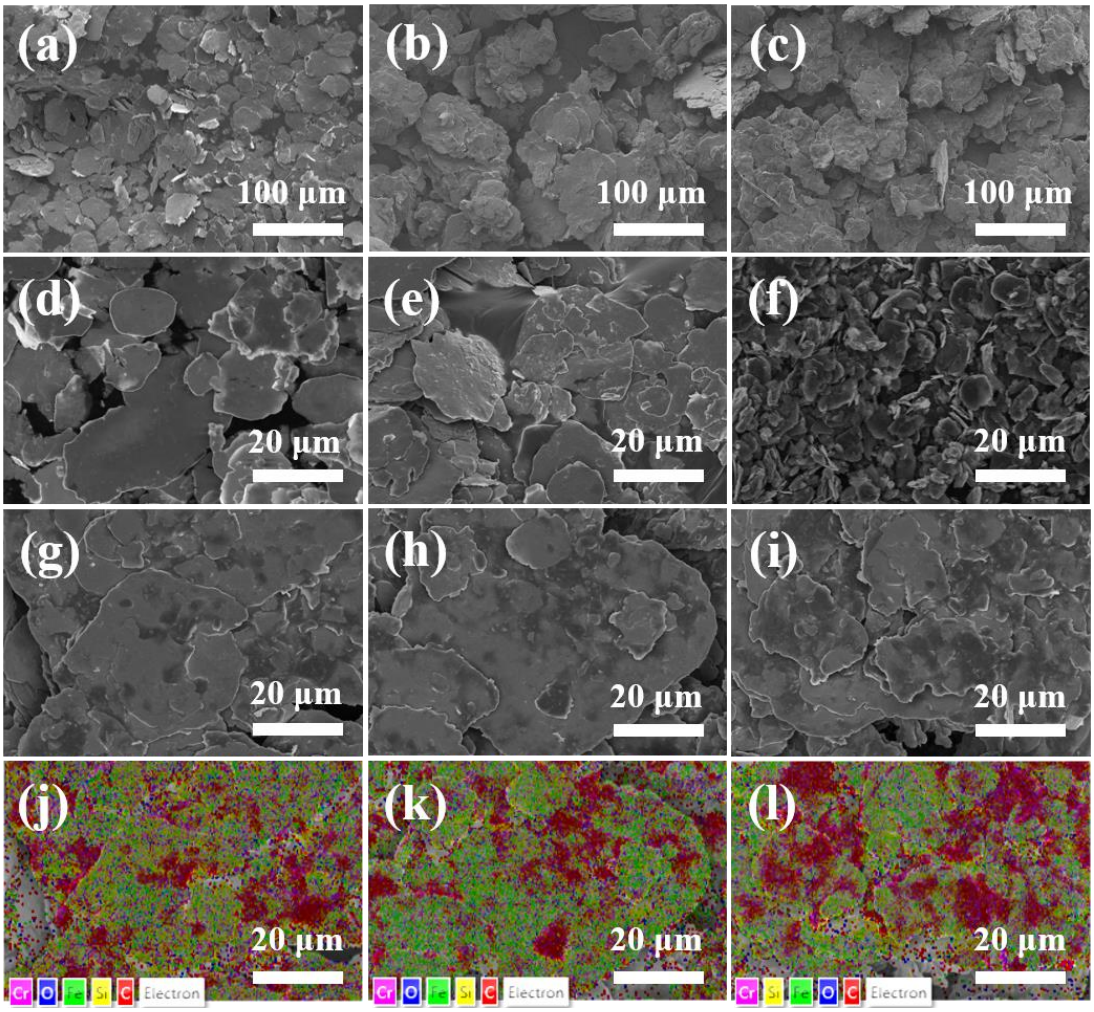

Figure 3. Low-magnification SEM images of (**a**) FFSC, (**b**) FFSC@E and (**c**) FFSC@G_{2000}/E; high-magnification SEM images of (**d**) FFSC, (**e**) FFSC@E, (**f**) G_{2000}, (**g**) FFSC@G_{1200}/E, (**h**) FFSC@G_{2000}/E and (**i**) FFSC@G_{5000}/E; elemental mappings of (**j**) FFSC@G_{1200}/E, (**k**) FFSC@G_{2000}/E and (**l**) FFSC@G_{5000}/E.

The EM parameters of FFSC@G/E were studied. They include complex permittivity ($\varepsilon_r = \varepsilon' - j\varepsilon''$) and complex permeability ($\mu_r = \mu' - j\mu''$). The real parts of complex permeability (μ') and complex permittivity (ε') represent the energy storage capacity of the absorbent with respect to the incident wave, while the imaginary parts of the EM parameters (μ'' and ε'') are related to the loss to microwave energy. As shown in Figure 5, all the EM parameters and the loss angle tangent ($\tan\delta_\varepsilon = \varepsilon''/\varepsilon'$, $\tan\delta_\mu = \mu''/\mu'$) of the FFSC sample decreased significantly in the frequency range of 0.5–18 GHz after coating. According to the Maxwell–Garnett theory, FFSC is the component that mainly influences the EM parameters

in coaxial absorbers. The introduction of the graphite/epoxy coating led to a reduction of the volume fraction of FFSC [33].

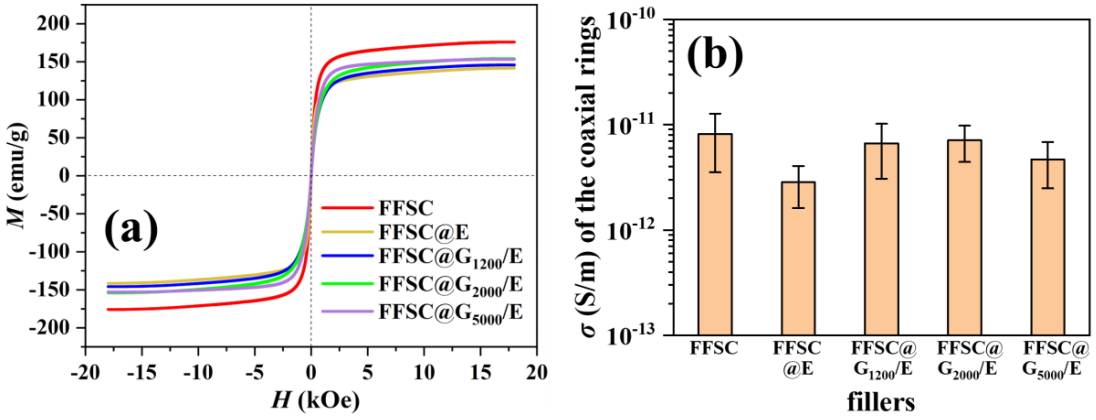

Figure 4. (**a**) Hysteresis loops of the magnetic powder samples and (**b**) conductivity of the coaxial ring samples filled with different magnetic powders.

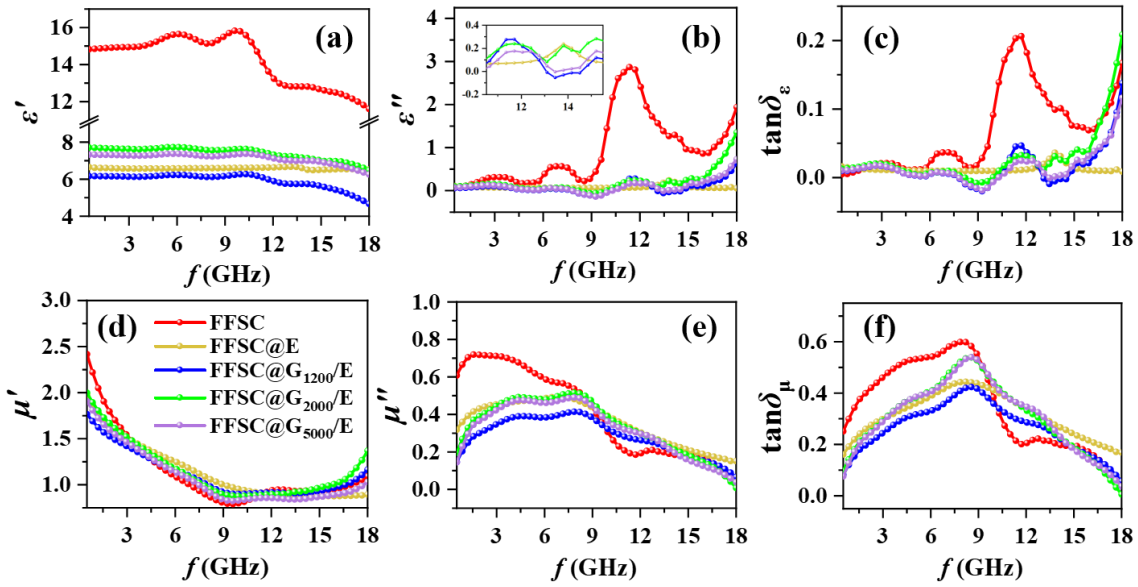

Figure 5. EM parameters of the magnetic powder samples: (**a**) real permittivity; (**b**) imaginary permittivity; (**c**) real permeability; (**d**) imaginary permeability; (**e**) dielectric loss tangent and (**f**) magnetic loss tangent.

The MAP of the magnetic powder samples was characterized by the reflection loss (RL) spectrum in accordance with the transmission line theory [19]:

$$\mathrm{RL(dB)} = 20\lg\left|\frac{Z_{\mathrm{in}} - Z_0}{Z_{\mathrm{in}} + Z_0}\right| \quad (1)$$

$$Z_{\mathrm{in}} = \sqrt{\frac{\mu_0\mu_{\mathrm{r}}}{\varepsilon_0\varepsilon_{\mathrm{r}}}}\tanh\left(\mathrm{j}\frac{2\pi f d}{c}\sqrt{\mu_{\mathrm{r}}\varepsilon_{\mathrm{r}}}\right) \quad (2)$$

where μ_0, ε_0, f, d and c are the permeability of free space, the permittivity of free space, the frequency of the incident wave, the thickness of the absorber and the wave velocity of free space, respectively.

Figure 6 shows the two-dimensional RL spectra of the magnetic powder samples; the zones of effective absorption surrounded by black lines represent RL < −10 dB, in which case over 90% of the incident wave was considered to be absorbed, while in the zone of RL < −20 dB

surrounded by a red line, over 99% of the incident wave could be absorbed. It can be observed that all spectra demonstrated the features of the quarter wavelength rule [27]:

$$d = \frac{\lambda}{4} = \frac{c}{4f\sqrt{|\mu_r \varepsilon_r|}} \quad (3)$$

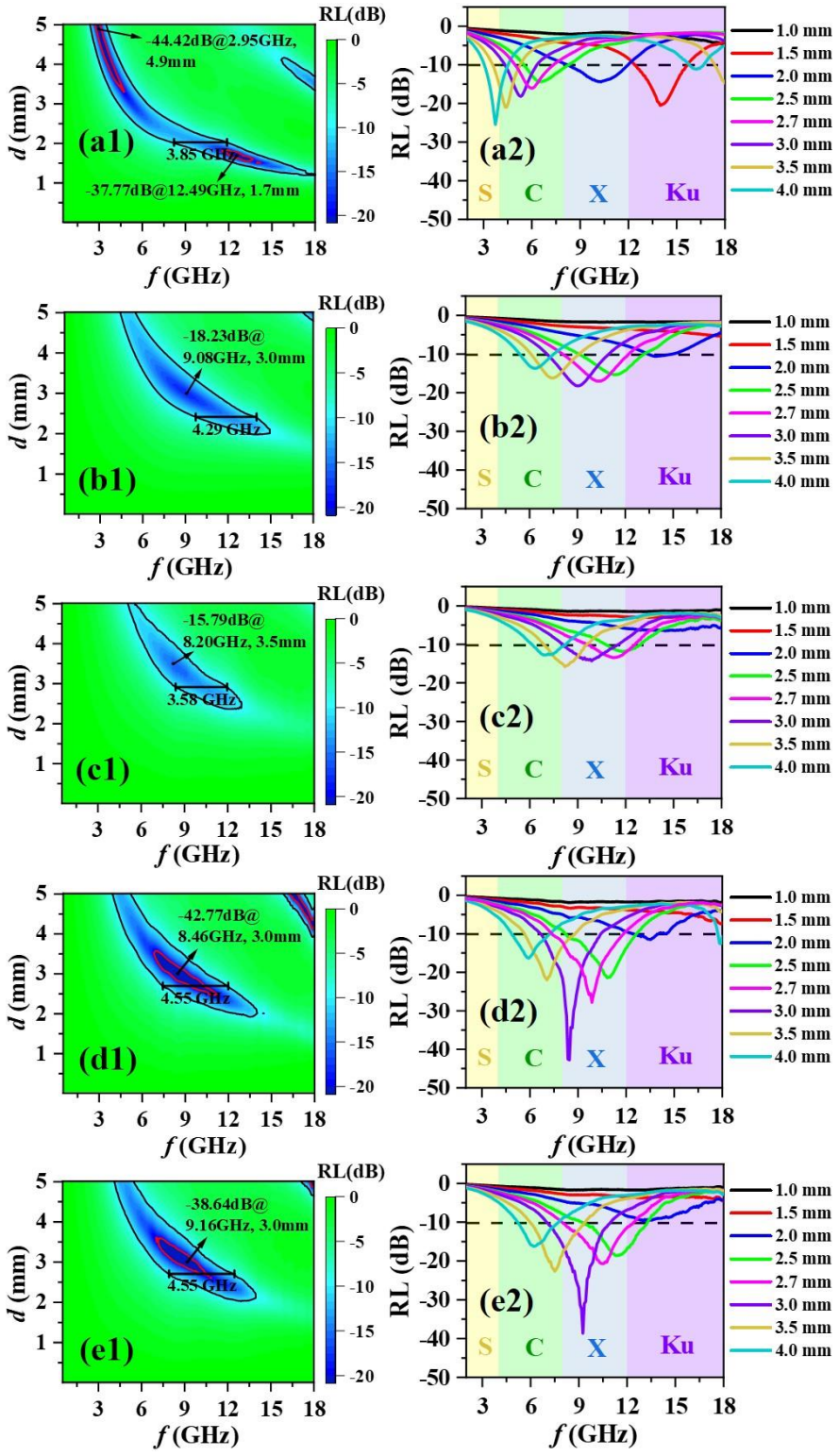

Figure 6. Two-dimension RL spectra of (**a1**,**a2**) FFSC, (**b1**,**b2**) FFSC@E, (**c1**,**c2**) FFSC@G_{1200}/E, (**d1**,**d2**) FFSC@G_{2000}/E and (**e1**,**e2**) FFSC@G_{5000}/E.

We observed that the matching thickness corresponding to RL_{min} decreased for higher frequency and the strong absorption zone moved towards higher frequencies and thicknesses for lower EM parameters after the coating of FFSC. For the original FFSC sample, two RL_{min} of −44.42 dB@4.9 mm and −37.77 dB@1.7 mm were separately located in the S band (2–4 GHz) and the Ku band (12–18 GHz), and the EAB_{max} reached 3.85 GHz (8.20–12.05 GHz) @2.0 mm (Figure 6a1,a2). For the FFSC@E and FFSC@G/E samples, the effective absorption regions were located in the C and the X bands (4–8 GHz and 8–12 GHz) (Figure 6b1,b2,c1,c2). Compared with the raw FFSC, the MAP of the FFSC@E and FFSC@G_{1200}/E samples worsened, while the FFSC@G_{2000}/E and FFSC@G_{5000}/E samples exhibited excellent MAP with an RL_{min} of −42.77 dB@3.0 mm and −38.64 dB@3.0 mm, respectively, and an identical EAB_{max} of 4.55 GHz@2.7 mm (7.33–11.88 GHz and 7.85–12.40 GHz) (Figure 6d1,d2,e1,e2).

The MAP of materials include impedance matching performance and attenuation properties. To fully absorb an incident microwave, the prerequisite of impedance matching must be met, i.e., the incident wave should enter the absorber to the full extent. The degree of impedance matching is measured by the delta value spectrum ($|\Delta|$) combined with the quarter wavelength curve, and the $|\Delta|$ is expressed by the following equations [25,34]:

$$|\Delta| = |\sinh^2(Kfd) - M| \tag{4}$$

$$K = \frac{4\pi\sqrt{\mu'\varepsilon'}}{c}\frac{\sin\left(\frac{\delta_\mu+\delta_\varepsilon}{2}\right)}{\cos\delta_\mu\cos\delta_\varepsilon} \tag{5}$$

$$M = \frac{4\mu'\varepsilon'\cos\delta_\mu\cos\delta_\varepsilon}{\left(\mu'\cos\delta_\varepsilon - \varepsilon'\cos\delta_\mu\right)^2 + \tan\left(\frac{\delta_\mu-\delta_\varepsilon}{2}\right)\left(\mu'\cos\delta_\varepsilon + \varepsilon'\cos\delta_\mu\right)^2} \tag{6}$$

where δ_ε and δ_μ are the dielectric loss angle and the magnetic loss angle, respectively. Better impedance matching is obtained by increasing the degree of overlap between the area of $|\Delta| < 0.2$ and quarter wavelength curve [34,35]. As shown in Figure 7a, the original FFSC had the largest area of $|\Delta| < 0.2$, but the $|\Delta| < 0.2$ area overlapping with the quarter wavelength curve was significantly small. A complete separation of $|\Delta| < 0.2$ areas and quarter wavelength curves is shown in the spectra of the FFSC@E and FFSC@G_{1200}/E samples (Figure 7b,c), which accounted for their poor MAP (Figure 6b1,b2,c1,c2). As for the FFSC@G_{2000}/E and FFSC@G_{5000}/E samples, the overlapping areas were highly consistent with their strong absorption region in the RL spectra (Figures 6d1,d2,e1,e2 and 7d,e). Therefore, the impedance matching performance plays an essential role in determining the MAP of FFSC@G/E samples.

The attenuation properties were measured by the attenuation constant (α) expressed by Equation (7) [28,36]. The higher values of α indicated better attenuation properties, and it was shown that a high value of α requires larger imaginary EM parameters.

$$\alpha = \frac{\sqrt{2}\pi f}{c}\sqrt{\left(\mu''\varepsilon'' - \mu'\varepsilon'\right) + \sqrt{\left(\mu''\varepsilon'' - \mu'\varepsilon'\right)^2 + \left(\mu''\varepsilon' + \mu'\varepsilon''\right)^2}} \tag{7}$$

As shown in Figure 8, the value of α of uncoated FFSC decreased after coating as a result of the simultaneous decrease in ε'' and μ'' (Figure 5b,d). Apart from this, the FFSC@G_{2000}/E and FFSC@G_{5000}/E samples still showed relatively high α values among the coated FFSC samples. Similar to the result of the $|\Delta|$ spectra (Figure 7d,e), the frequency ranges corresponding to the peaks in the α spectra were consistent with regions of low RL (Figure 6d1,d2,e1,e2). These results suggested that the synergy of high-impedance matching performance and attenuation properties in the X band contributed to the good MAP of the FFSC@G_{2000}/E and FFSC@G_{5000}/E samples.

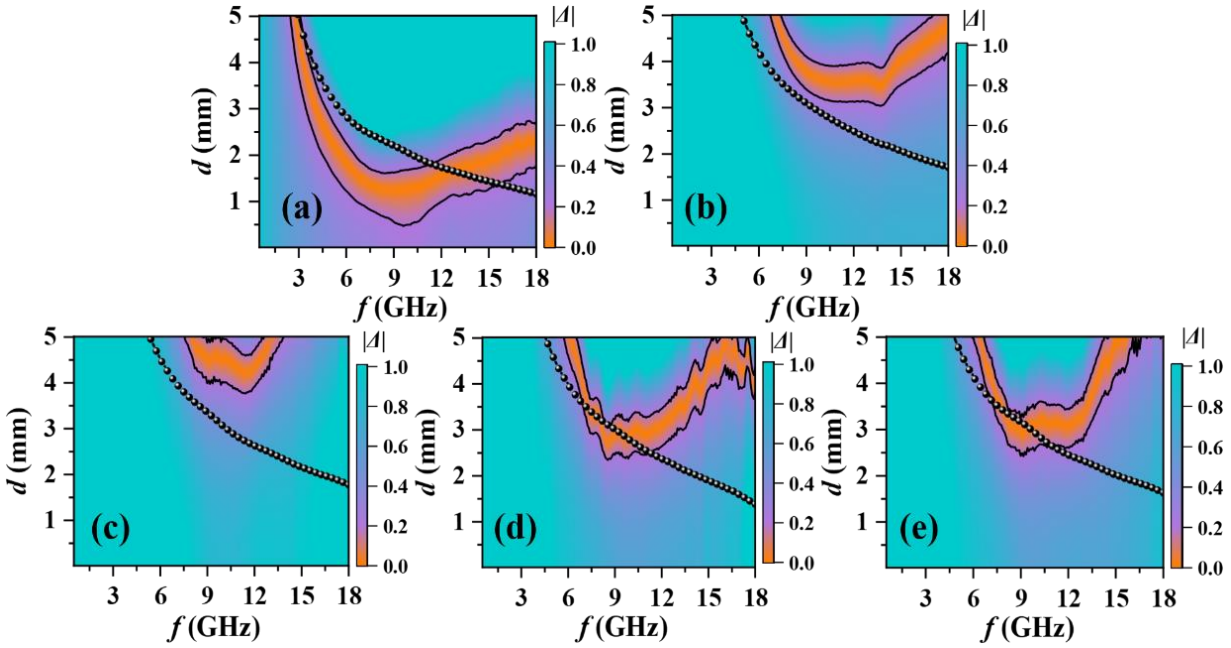

Figure 7. Delta spectra and quarter wavelength curves of (**a**) FFSC, (**b**) FFSC@E, (**c**) FFSC@G_{1200}/E, (**d**) FFSC@G_{2000}/E and (**e**) FFSC@G_{5000}/E.

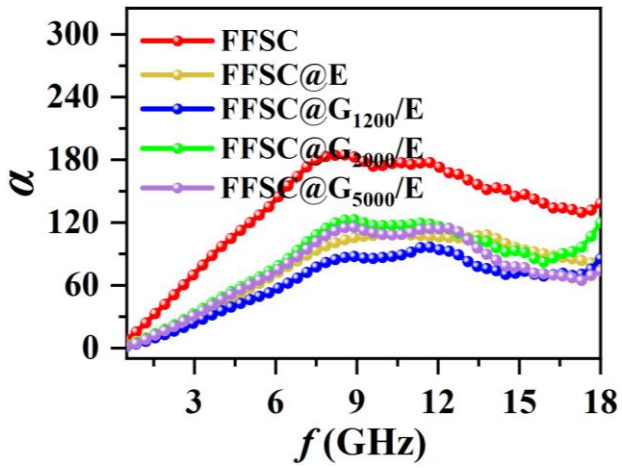

Figure 8. Attenuation constant spectra of the magnetic powder samples.

The possible microwave absorption mechanisms of FFSC@G/E sample are illustrated in Figure 9. Firstly, multiple polarization processes took place at the enriched interfaces of FFSC/graphite, FFSC/epoxy and epoxy/graphite. Secondly, the defects existing in the graphite provided dipolar polarization loss. Thirdly, the sub-centimeter paraffin-based absorber loaded with FFSC@G/E dissipated the incident microwave through multiple scattering and reflection [37]. Fourthly, magnetic loss was generated by FFSC with its intrinsic ferromagnetism. These loss mechanisms contributed to the excellent MAP of FFSC@G_{2000}/E and FFSC@G_{2000}/E.

As shown in Table 1, compared with other ferromagnetic X-band absorbents, the FFSC@G_{2000}/E and FFSC@G_{2000}/E samples had lower RL_{min} and larger bandwidth, owing to their better impedance matching. Compared with other carbon-coated X-band absorbents, the FFSC@G_{2000}/E and FFSC@G_{2000}/E samples had lower filler loading and smaller thickness because of their reduced density after coating.

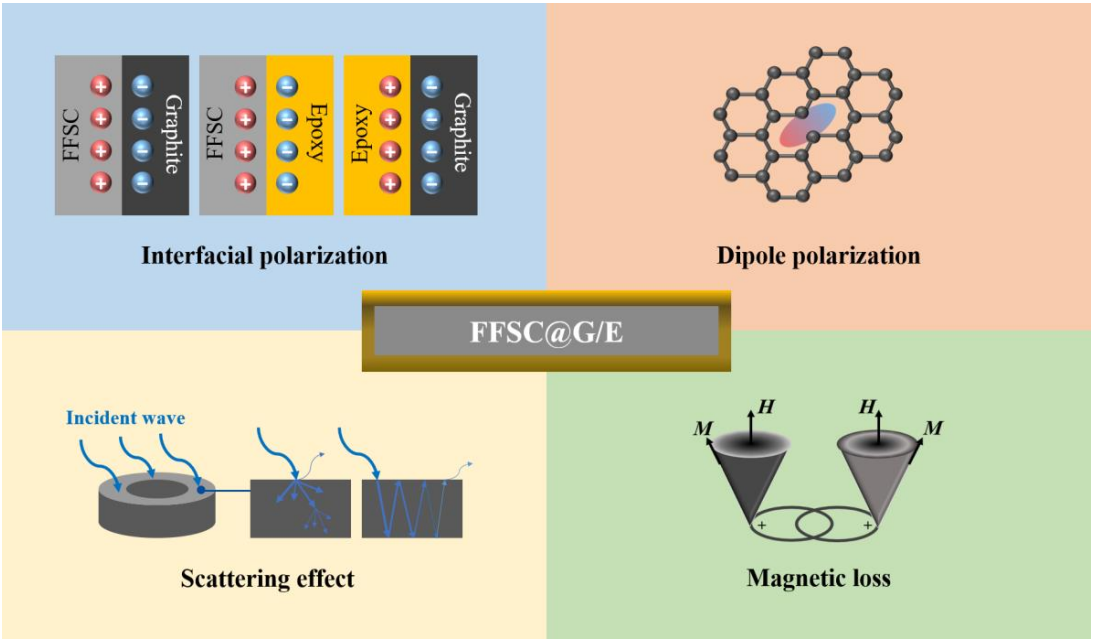

Figure 9. Schematic illustration of the microwave absorption mechanisms of FFSC@G/E.

Table 1. Comparison of the recently reported X-band MAMs with FFSC@G/E.

Materials	Loading	RL_{min}	EAB_{max}	References
$FeCoNiAlCr_{0.9}$	50 wt.%	−29.7 dB@2 mm	4.28 GHz@2 mm	[12]
$Fe@CN_x$	50 wt.%	−26.8 dB	-	[25]
$SnO_2/Sn/rGO$	5 wt.%	−39.5 dB@3.0 mm	-	[38]
$MnFe_2O_4/rGO/Diatomite$	80 wt.%	−76.6 dB@2.5 mm	3.61 GHz@2.5 mm	[39]
$MoSe_2$@rGO	40 wt.%	−56.9 dB@8.9 mm	4.12 GHz@8.9 mm	[40]
$ANF/MWCNT/Fe_3O_4$	-	−45.8 dB@3.7 mm	4.0 GHz@1.4 mm	[41]
$Sr_3Co_2Fe_{24}O_{41}/MoS_2$	60 wt.%	−44.5 dB@3.0 mm	3.92 GHz@3.0 mm	[42]
$FFSC@G_{2000}/E$	30 wt.%	−42.8 dB@3.0 mm	4.55 GHz@2.7 mm	This work
$FFSC@G_{5000}/E$	30 wt.%	−38.6 dB@3.0 mm	4.55 GHz@2.7 mm	This work

4. Conclusions

To conclude, a core–shell structure of graphite-and epoxy-coated flaky magnetic FFSC@G/E particles was prepared by solution blending under room temperature. Compared with the original FFSC, $FFSC@G_{2000}/E$ exhibited higher absorption properties in the X band, and its RL_{min} remained at −42.77 dB with the reduction of thickness from 4.9 mm to 3.0 mm. The effective absorption bandwidth increased from 3.85 GHz to 4.55 GHz at a thickness of 2.7 mm. The enhancement of the MAP after graphite/epoxy coating was attributed to an improvement in impedance matching, as well as to various loss mechanisms such as relaxation polarization and magnetic loss in the heterostructures. Hence, this work produced and presented a novel class of magnetic–electric MAMs.

Author Contributions: Conceptualization, methodology, investigation, writing—original draft preparation, H.Z.; Conceptualization, supervision, writing—review and editing, X.Z.; Methodology, formal analysis, data curation, J.H., N.H. and H.X.; Software, Resources, Validation, X.L. and Q.Z.; Writing—review & editing Z.L. and R.V.R. All authors have read and agreed to the published version of the manuscript.

Funding: This work was supported by the Special project of Foshan scientific and technological innovation team (Grant Numbers: 2030032000171, 2120001010823). This research was also supported by the Singapore-HUJ Alliance for Research and Enterprise (SHARE), the Nanomaterials for Energy and Energy-Water Nexus (NEW), the Campus for Research Excellence and Technological Enterprise (CREATE), Singapore 138602.

Data Availability Statement: The data used to support the findings of this study are available from the corresponding author upon request.

Conflicts of Interest: The authors declare that they have no known competing financial interests or personal relationships that could influence the work reported in this paper.

References

1. Pang, H.; Duan, Y.; Huang, L.; Song, L.; Liu, J.; Zhang, T.; Yang, X.; Liu, J.; Ma, X.; Di, J.; et al. Research advances in composition, structure and mechanisms of microwave absorbing materials. *Compos. Part B* **2021**, *224*, 109173. [CrossRef]
2. Peng, K.; Liu, C.; Wu, Y.; Fang, G.; Xu, G.; Zhang, Y.; Wu, C.; Yan, M. Understanding the efficient microwave absorption for FeCo@ZnO flakes at elevated temperatures a combined experimental and theoretical approach. *J. Mater. Sci. Technol.* **2022**, *125*, 212–221. [CrossRef]
3. Wang, B.; Wu, Q.; Fu, Y.; Liu, T. A review on carbon/magnetic metal composites for microwave absorption. *J. Mater. Sci. Technol.* **2021**, *86*, 91–109. [CrossRef]
4. Weng, X.; Li, B.; Zhang, Y.; Lv, X.; Gu, G. Synthesis of flake shaped carbonyl iron/reduced graphene oxide/polyvinyl pyrrolidone ternary nanocomposites and their microwave absorbing properties. *J. Alloys Compd.* **2017**, *695*, 508–519. [CrossRef]
5. Zhang, X.; Guo, Y.; Ali, R.; Tian, W.; Liu, Y.; Zhang, L.; Wang, X.; Zhang, L.; Yin, L.; Su, H.; et al. Bifunctional carbon-encapsulated FeSiAl hybrid flakes for enhanced microwave absorption properties and analysis of corrosion resistance. *J. Alloys Compd.* **2020**, *828*, 154079. [CrossRef]
6. Chen, Y.; Wang, L.; Xiong, H.; Rehman, S.; Tan, Q.; Huang, Q.; Zhong, Z. Optimized Absorption Performance of FeSiCr Nanoparticles by Changing the Shape Anisotropy. *Phys. Status Solidi A* **2020**, *217*, 2000389. [CrossRef]
7. Wang, L.; Xiong, H.; Rehman, S.; Tan, Q.; Chen, Y.; Zhang, L.; Yang, J.; Wu, F.; Zhong, M.; Zhong, Z. Microwave absorbing property enhancement of FeSiCr nanomaterials by regulating nanoparticle size. *J. Alloys Compd.* **2019**, *803*, 631–636. [CrossRef]
8. Acher, O.; Adenot, A. Bounds on the dynamic properties of magnetic materials. *Phys. Rev. B* **2000**, *62*, 11324. [CrossRef]
9. Walser, R.; Win, W.; Valanju, P. Shape-optimized ferromagnetic particles with maximum theoretical microwave susceptibility. *IEEE Trans. Magn.* **1998**, *34*, 1390–1392. [CrossRef]
10. Guan, Z.; Wang, Z.; Jiang, J.; Gong, Y.; Yao, Y.; Zhen, L. Flaky FeSi particles with tunable size, morphology and microstructure developing for high-efficiency and broadband absorbing materials. *J. Magn. Magn. Mater.* **2021**, *527*, 167800. [CrossRef]
11. Yang, W.; Zhang, Y.; Qiao, G.; Lai, Y.; Liu, S.; Wang, C.; Han, J.; Du, H.; Zhang, Y.; Yang, Y.; et al. Tunable magnetic and microwave absorption properties of $Sm_{1.5}Y_{0.5}Fe_{17-x}Si_x$ and their composites. *Acta Mater.* **2018**, *145*, 331–336. [CrossRef]
12. Duan, Y.; Pang, H.; Wen, X.; Zhang, X.; Wang, T. Microwave absorption performance of $FeCoNiAlCr_{0.9}$ alloy powders by adjusting the amount of process control agent. *J. Mater. Sci. Technol.* **2020**, *77*, 209–216. [CrossRef]
13. Min, D.; Zhou, W.; Qing, Y.; Luo, F.; Zhu, D. Highly oriented flake carbonyl iron/carbon fiber composite as thin-thickness and wide-bandwidth microwave absorber. *J. Alloys Compd.* **2018**, *744*, 629–636. [CrossRef]
14. Peng, K.; Wu, Y.; Liu, C.; Xu, G.; Fang, G.; Zhang, Y.; Cao, Y.; Zhang, Y. The tunable microwave absorption performance of the oriented flaky Fe-Co-Nd with a broad bandwidth absorption at a thin thickness. *J. Magn. Magn. Mater.* **2020**, *510*, 166925. [CrossRef]
15. Zhou, X.; Jia, Z.; Zhang, X.; Wang, B.; Wu, W.; Liu, X.; Xu, B.; Wu, G. Controllable synthesis of Ni/NiO@porous carbon hybrid composites towards remarkable electromagnetic wave absorption and wide absorption bandwidth. *J. Mater. Sci. Technol.* **2021**, *87*, 120–132. [CrossRef]
16. Tian, W.; Zhang, X.; Guo, Y.; Mu, C.; Zhou, P.; Yin, L.; Zhang, L.; Zhang, L.; Lu, H.; Jian, X.; et al. Hybrid silica-carbon bilayers anchoring on FeSiAl surface with bifunctions of enhanced anti-corrosion and microwave absorption. *Carbon* **2021**, *173*, 185–193. [CrossRef]
17. Ren, Y.; Zhang, Y.; Zheng, Q.; Wang, L.; Jiang, W. Integrating large specific surface area and tunable magnetic loss in Fe@C composites for lightweight and high-efficiency electromagnetic wave absorption. *Carbon* **2023**, *206*, 226–236. [CrossRef]
18. He, N.; Yang, X.; Shi, L.; Yang, X.; Lu, Y.; Tong, G.; Wu, W. Chemical conversion of Cu_2O/PPy core-shell nanowires (CSNWs): A surface/interface adjustment method for high-quality Cu/Fe/C and Cu/Fe_3O_4/C CSNWs with superior microwave absorption capabilities. *Carbon* **2020**, *166*, 205–217. [CrossRef]
19. Liu, Z.; Wang, Y.; Jia, Z.; Ling, M.; Yan, Y.; Chai, L.; Du, H.; Wu, G. In situ constructed honeycomb-like $NiFe_2O_4$@Ni@C composites as efficient electromagnetic wave absorber. *J. Colloid Interface Sci.* **2022**, *608*, 2849–2859. [CrossRef]
20. Shen, Z.; Yang, H.; Xiong, Z.; Xie, Y.; Liu, C. Hollow core-shell CoNi@C and CoNi@NC composites as high-performance microwave absorbers. *J. Alloys Compd.* **2021**, *871*, 159574. [CrossRef]
21. Ge, J.; Liu, S.; Liu, L.; Cui, Y.; Meng, F.; Li, Y.; Zhang, X.; Wang, F. Optimizing the electromagnetic wave absorption performance of designed hollow $CoFe_2O_4$/CoFe@C microspheres. *J. Mater. Sci. Technol.* **2021**, *81*, 190–202. [CrossRef]
22. Li, Q.; Tan, J.; Wu, Z.; Wang, L.; You, W.; Wu, L.; Che, R. Hierarchical magnetic-dielectric synergistic Co/CoO/RGO microspheres with excellent microwave absorption performance covering the whole X band. *Carbon* **2023**, *201*, 150–160. [CrossRef]
23. Zhao, H.; Wang, F.; Cui, L.; Xu, X.; Han, X.; Du, Y. Composition optimization and microstructure design in MOFs-derived magnetic carbon-based microwave absorbers: A review. *Nano-Micro Lett.* **2021**, *13*, 208. [CrossRef] [PubMed]

24. Yang, X.; Duan, Y.; Li, S.; Huang, L.; Pang, H.; Ma, B.; Wang, T. Constructing three-dimensional reticulated carbonyl iron/carbon foam composites to achieve temperature-stable broadband microwave absorption performance. *Carbon* **2022**, *188*, 376–384. [CrossRef]
25. Zhang, Z.; Li, Y.; Liao, Y.; Rong, H.; Zhang, W.; Zhang, M.; Qin, G.; Zhang, X. Synthesizing CN_x heterostructures on ferromagnetic nanoparticles for improving microwave absorption property. *Appl. Surf. Sci.* **2021**, *564*, 150480. [CrossRef]
26. Chen, J.; Lei, W.; Huang, C.; Wang, J.; Zhang, Y.; Liu, Z.; Xu, Z.; Wang, K.; Guo, S. Magneto-electric adjustable Co/C porous layer coated flaky carbonyl iron composites with bifunctions of anti-corrosion and microwave absorption. *J. Alloys Compd.* **2022**, *927*, 167104. [CrossRef]
27. Wu, Z.; Cheng, H.; Jin, C.; Yang, B.; Xu, C.; Pei, K.; Zhang, H.; Yang, Z.; Che, R. Dimensional design and core–shell engineering of nanomaterials for electromagnetic wave absorption. *Adv. Mater.* **2022**, *34*, 2107538. [CrossRef]
28. Cheng, J.; Zhang, H.; Xiong, Y.; Gao, L.; Wen, B.; Raza, H.; Wang, H.; Zheng, G.; Zhang, D.; Zhang, H. Construction of multiple interfaces and dielectric/magnetic heterostructures in electromagnetic wave absorbers with enhanced absorption performance: A review. *J. Mater.* **2021**, *7*, 1233–1263. [CrossRef]
29. Wang, F.; Dong, Y.; Chang, L.; Pan, Y.; Chi, Q.; Gong, M.; Li, J.; He, A.; Wang, X. High performance of Fe-based soft magnetic composites coated with novel nano-$CaCO_3$/epoxy nanocomposites insulating layer. *J. Solid State Chem.* **2021**, *304*, 122634. [CrossRef]
30. Wang, Q.; Niu, B.; Han, Y.; Zheng, Q.; Li, L.; Cao, M. Nature-inspired 3D hierarchical structured "vine" for efficient microwave attenuation and electromagnetic energy conversion device. *Chem. Eng. J.* **2022**, *452*, 139042. [CrossRef]
31. Feng, Y.; Xia, L.; Ding, C.; Yan, H.; Xu, G.; Zhang, T.; Xiong, L.; Qin, C.; Wen, G. Boosted multi-polarization from silicate-glass@rGO doped with modifier cations for superior microwave absorption. *J. Colloid Interface Sci.* **2021**, *593*, 96–104. [CrossRef] [PubMed]
32. Wang, L.; Yu, X.; Li, X.; Zhang, J.; Wang, M.; Che, R. Conductive-network enhanced microwave absorption performance from carbon coated defect-rich Fe_2O_3 anchored on multi-wall carbon nanotubes. *Carbon* **2019**, *15*, 298–308. [CrossRef]
33. Yan, L.; Wang, Y.; Li, W.; Liao, Z.; Wang, X.; Huang, W.; Zhang, L.; Li, Y. Lightweight and salt spray corrosion resistant porous SiC/FeSiCr hybrids for enhanced microwave absorption in the C-band. *J. Alloys Compd.* **2022**, *907*, 164467. [CrossRef]
34. Ma, Z.; Cao, C.; Liu, Q.; Wang, J. A New Method to Calculate the Degree of Electromagnetic Impedance Matching in One-Layer Microwave Absorbers. *Chin. Phys. Lett.* **2012**, *29*, 038401. [CrossRef]
35. Hu, J.; Liu, S.; Wang, Y.; Ju, W.; He, N.; He, J.; Jia, H.; Xia, C.; Huang, Z.; Long, J.; et al. Manganese phosphate coated flaky FeSiAl powders with enhanced microwave absorbing properties and improved corrosion resistance. *Mater. Chem. Phys.* **2023**, *296*, 127274. [CrossRef]
36. Lu, B.; Huang, H.; Dong, X.; Zhang, X.; Lei, J.; Sun, J.; Dong, C. Influence of alloy components on electromagnetic characteristics of core/shell-type Fe–Ni nanoparticles. *J. Appl. Phys.* **2008**, *104*, 114313. [CrossRef]
37. Huynen, I. Investigation of microwave absorption mechanisms in microcellular foamed conductive composites. *Micro* **2021**, *1*, 86–101. [CrossRef]
38. Li, T.; Wang, C.; An, Y.; Xia, Y.; Wang, X.; Huang, X. Tunable and ultraefficient microwave absorptivity in SnO_2/Sn/rGO composites via enhanced polarization effect. *J. Alloys Compd.* **2022**, *930*, 167250. [CrossRef]
39. Li, Q.; Guo, W.; Kong, X.; Xu, J.; Xu, C.; Chen, Y.; Chen, J.; Jia, X.; Ding, Y. $MnFe_2O_4$/rGO/Diatomite composites with excellent wideband electromagnetic microwave absorption. *J. Alloys Compd.* **2023**, *941*, 168851. [CrossRef]
40. Fu, X.; Zheng, Q.; Li, L.; Cao, M. Vertically implanting $MoSe_2$ nanosheets on the RGO sheets towards excellent multi-band microwave absorption. *Carbon* **2022**, *197*, 324–333. [CrossRef]
41. Ma, Y.; Li, Y.; Zhao, X.; Zhang, L.; Wang, B.; Nie, A.; Mu, C.; Xiang, J.; Zhai, K.; Xue, T.; et al. Lightweight and multifunctional superhydrophobic aramid nanofiber/multiwalled carbon nanotubes/Fe_3O_4 aerogel for microwave absorption, thermal insulation and pollutants adsorption. *J. Alloys Compd.* **2022**, *919*, 165792. [CrossRef]
42. Zhang, M.; Qian, C.; Zhu, R.; Liu, H.; Zhang, Y.; Liu, Q. Flower-like MoS_2 self-assembled on multiferroic Z-type $Sr_3Co_2Fe_{24}O_{41}$ hexaferrite for ultra-wideband microwave absorption. *J. Alloys Compd.* **2022**, *926*, 166881. [CrossRef]